Supporting Information

Manipulating a vertical temperature-gradient of Fe@Enteromorpha/graphene aerogel to enhanced solar evaporation and sterilization

Yan Kong [a], Yue Gao *[a], Yunkai Sun [a], Yuanfeng Qi [b], Weiyan Yin [c], Shouquan Wang [d], Fengjiao Yin [d], Zhenguo Dai [e], Baoyu Gao [a], Qinyan Yue *[a]

a. Shandong Key Laboratory of Water Pollution Control and Resource Reuse, School of Environmental Science and Engineering, Shandong University, Qingdao 266000, PR China

b. School of Environmental and Municipal Engineering, Qingdao University of Technology, Qingdao 266033, PR China

c. Hubei Key Laboratory of Biomass Fibers and Eco-dyeing & Finishing, School of Chemistry and Chemical Engineering, Wuhan Textile University

d. Shandong Tianli Energy Co., Ltd

e. Shandong Shanda WIT Science and Technology Co., Ltd., Jinan 250061, Shandong, PR China

* Corresponding author. E-mail address: gaoyue0322@aliyun.com (Yue Gao). qyyue58@aliyun.com (Qinyan Yue).

This supplement contains:

1 Experimental Section

SI-1 Preparation of Graphene oxide (GO)

GO was synthesized by the oxidation of Graphite powder according to the modified Hummer's method: in brief, 3.0 g graphite powder, 18.0 g $KMnO_4$, and a mixture of concentrated H_2SO_4 and H_3PO_4 (V: V=360:40) were placed in a flask and stirred magnetically. The mixture was heated to 50^{o}C and kept at this temperature for 12 h. Then the reaction was cooled to room temperature and poured onto the ice with H_2O_2 (30%, 3 mL). The mixture was filtered and washed with 200 mL of 30% HCl and 200 mL of H_2O, respectively. Finally, the GO was obtained by drying in a vacuum for 24 h.

SI-2 Disinfection experiments

The bactericidal capacity of the MFeG aerogel solar evaporator was tested by using Escherichia coli (E. coli), a typical Gram-negative bacterium. Briefly, E. coli strains were cultured in tryptone soybean broth (TSB) with an orbital shaker at 37°C for 12 h. The bacteria were collected after centrifugation and washed 3 times with fresh PBS (0.01 M, pH 7.4), then diluted with PBS. The final concentration of E. coli *was* about 10^6 CFU/mL. In a typical experiment, the light intensity was changed (0, 1, 2, 5 suns), 20 mg of 8MFeG aerogel was floated in 20 mL of E. coli solution and placed on a magnetic stirrer. 500 μL of E. coli solution

from the top of the aerogel were collected at different intervals of time (0, 5, 10, 20, 30, 40, 50, 60 min) and diluted with PBS. 50 μL of the dilutes bacteria solution was smeared onto a Tryptose Soya Agar (TSA) to quantitate bacterial enumeration. For comparison, the control groups were put in darkness. All results were repeated in triplicates. The bactericidal efficiency (η) was calculated by the following equation:

$$\eta = \frac{N_i - N_r}{N_i} \quad \text{(S1)}$$

where N_i is the initial number of E. coli, and N_r is the residual number of E. coli.

SI-3 Estimation of heat loss

The heat loss by the absorber consists of three losses: (i) radiation, (ii) convection, and (iii) conduction. The details of the calculation are shown below:

Radiation

$$\Phi = \varepsilon A \sigma (T_1^4 - T_0^4) \quad \text{(S2)}$$

where Φ denotes heat flux, ε is the emissive rate, A is surface area, σ is the Stefan-Boltzmann constant (5.67×10^{-8} W m^{-2} K^{-4}), and T_1 represents the surface temperature of the solar steam generator after steady steam generation under illumination. T_0 is the ambient temperature near the light absorber/air interface.

Convection

$$Q = hA\Delta T \quad \text{(S3)}$$

where denotes the heat, h is convection heat transfer coefficient (5 $W \cdot m^{-2} \cdot K^{-1}$), A is surface area, ΔT is the difference between the absorber and ambient temperature in our experiment.

Conductive

$$Q = Cm\Delta T \quad \text{(S4)}$$

where Q denotes the heat, C is the specific heat capacity of water (4.18 J/g per °C), t is the irradiation time, m is the water weights, and ΔT is the elevated water temperature within t seconds. Based on the experiment, t = 3600 s, m = 50 g. The conduction loss refers to the heat from MFeG aerogel to bulk water rather than the heat from the system to an ambient environment.

Steady-state energy balance analysis:

For the MFeG aerogel solar evaporator, the top of the evaporator mainly includes heat conduction loss, heat convection loss, heat radiation loss, and also includes heat radiation and heat convection generated by the side of the aerogel due to the cold evaporation effect. Therefore, the energy exchange between the MFeG aerogel solar evaporator and the environment was analyzed using the following equation:

$$E_{\text{environment}} = \varepsilon A_1 \sigma (T_1^4 - T_0^4) + \varepsilon A_2 \sigma (T_2^4 - T_0^4) + hA_1(T_1 - T_0) + hA_2(T_2 - T_0) + C\text{m}\Delta T \qquad \text{(S5)}$$

where A_1 is the area of the top surface of the MFeG aerogel (3.14 cm^2), T_1 is the steady surface temperature of the top surface, T_0 is the ambient temperature (27°C), A_2 is the area of the side surface of the MFeG aerogel, T_2 is the surface temperature of the side surface.

Table S1. Experimental parameters and the calculated radiation flux and convection flux of the top surface

Evaporator height (mm)	Ambient temperature (°C)	Stable temperature (°C)	Radiation flux of the top surface (W)	Convection flux of the top surface (W)
0	27	40.4	0.026	0.021
2	27	41.5	0.029	0.023
4	27	41.7	0.029	0.023
6	27	42.1	0.030	0.024
8	27	40.9	0.027	0.022
10	27	40.1	0.026	0.021

15	27	39.1	0.024	0.019
20	27	37.9	0.021	0.017
25	27	37.4	0.020	0.016
35	27	36.4	0.018	0.015
45	27	35.5	0.016	0.013
55	27	35.3	0.016	0.013

Table S2. Experimental parameters and the calculated radiation flux and convection flux of the side surface

Evaporator height (mm)	Ambient temperature (°C)	Area of the side surface (cm^2)	Stable temperature (°C)	Radiation flux of the side surface (W)	Convection flux of the side surface (W)
0	27	0	0	0	0
2	27	1.26	32.4	0.004	0.003
4	27	2.51	33.7	0.010	0.008
6	27	3.77	32.3	0.012	0.010
8	27	5.02	30.1	0.009	0.008
10	27	6.28	31.5	0.017	0.014
15	27	9.42	29.8	0.016	0.013
20	27	12.56	29.1	0.016	0.013
25	27	15.70	24.7	-0.021	-0.018
35	27	21.98	24.6	-0.030	-0.026
45	27	28.26	24.5	-0.041	-0.035
55	27	34.54	24.5	-0.050	-0.043

Table S3. Experimental parameters and the calculated conduction

Evaporator height (mm)	Initial temperature of bulk water (°C)	Stable temperature of bulk water (°C)	Conduction flux (W)
0	26.4	27.3	0.052
2	26.4	26.8	0.023
4	26.4	26.9	0.029
6	26.4	26.8	0.023
8	26.4	26.8	0.023
10	26.4	26.7	0.017
15	26.4	26.6	0.012
20	26.4	26.4	0.000
25	26.4	26.4	0.000
35	26.4	26.2	-0.012
45	26.4	26.1	-0.017
55	26.4	25.8	-0.035

2 Supplemental Figure and Table

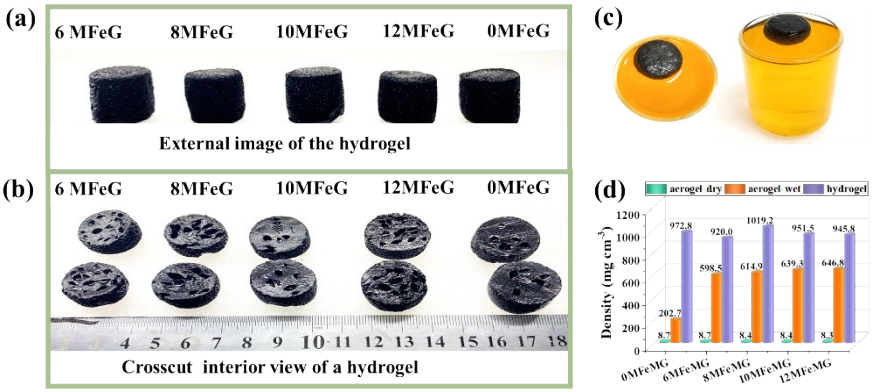

Figure S1. (a-b) Optical photograph of lotus root-like MFeG hydrogel, (c) photos of the MFeG aerogel floating on the water, (d) the density of MFeG aerogel in dry and wet state and hydrogel

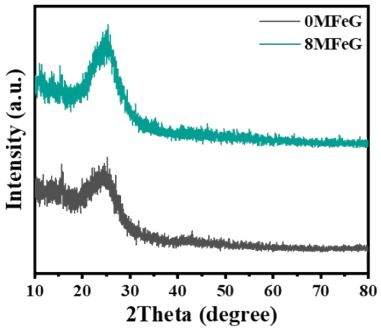

Figure S2. XRD patterns of 0MFeG and 8MFeG aerogel

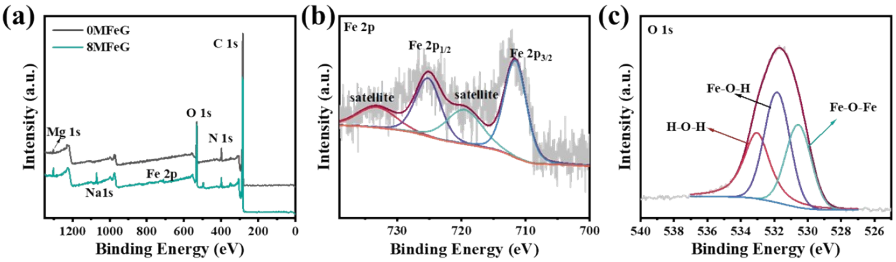

Figure S3. (a) XPS survey scan spectrum of the 0MFeG and 8MFeG aerogel, (b-c) high-resolution Fe 2p and O 1s spectrum of the 8MFeG aerogel

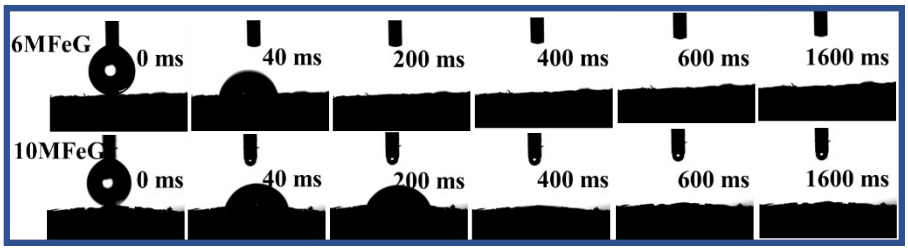

Figure S4. The contact angle image of 6MFeG and 10MFeG aerogel

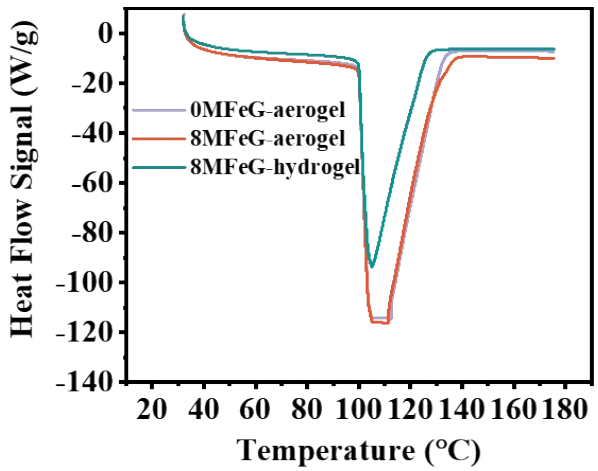

Figure S5. DSC analysis of the 0MFeG aerogel, 8MFeG aerogel, 8MFeG hydrogel

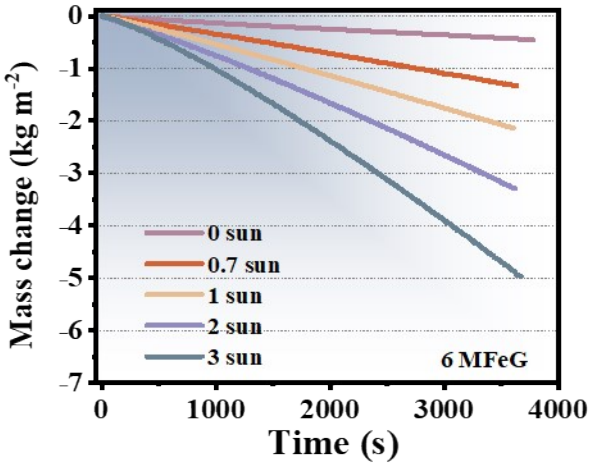

Figure S6. Mass change of water with 6MFeG aerogels over time under different sunlight intensity illumination

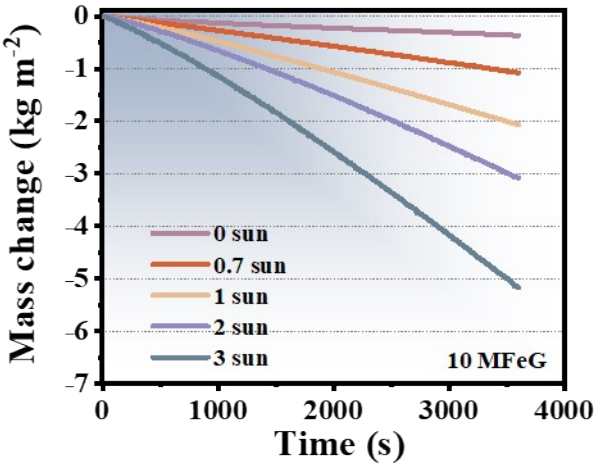

Figure S7. Mass change of water with 10MFeG aerogels over time under different sunlight intensity illumination

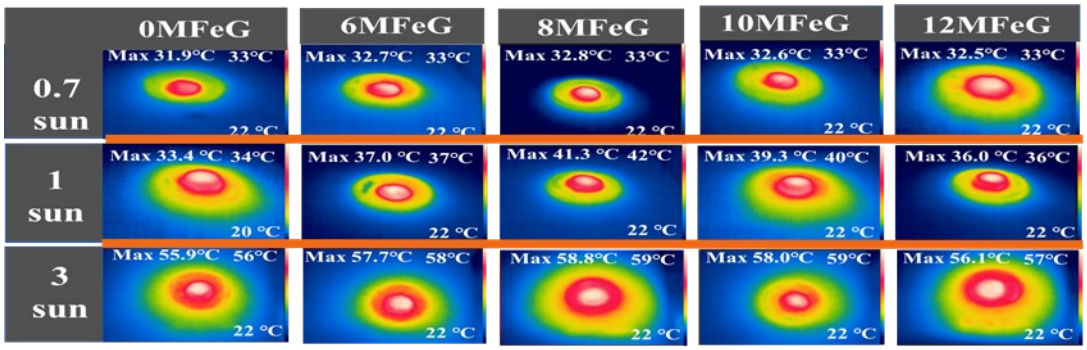

Figure S8. Infrared image of the MFeG aerogels under different sunlight intensity illumination

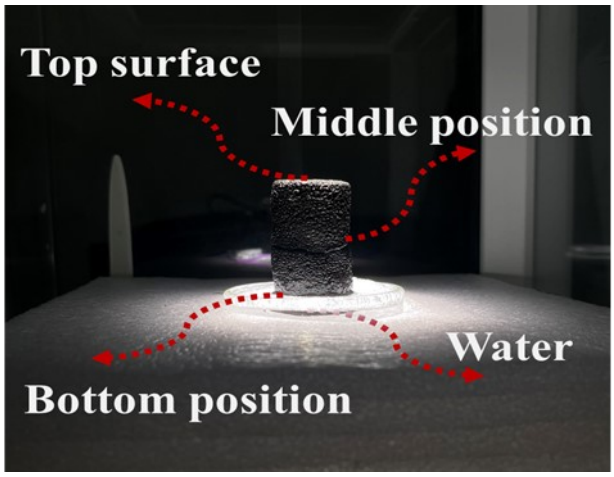

Figure S9. Schematic diagram of the positions for testing the temperature of the 8MFeG aerogel

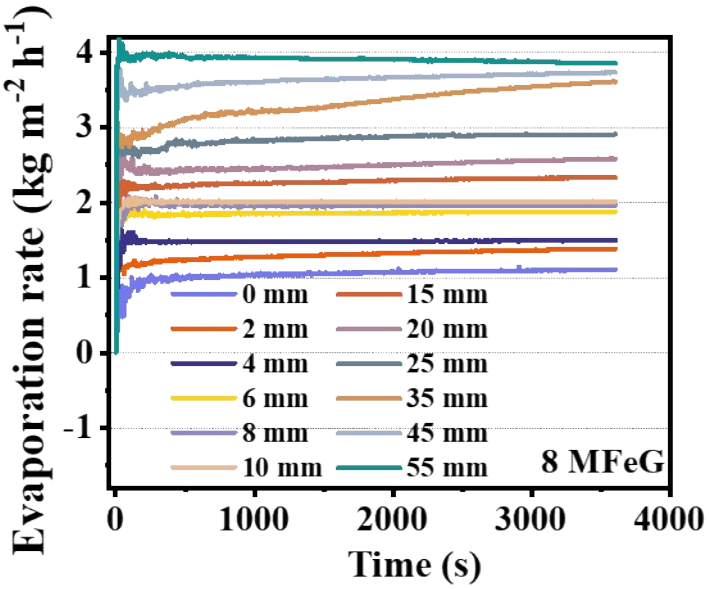

Figure S10. Evaporation rate of 8MFeG aerogels with 0-55 mm variable exposure heights under 1 sun illumination

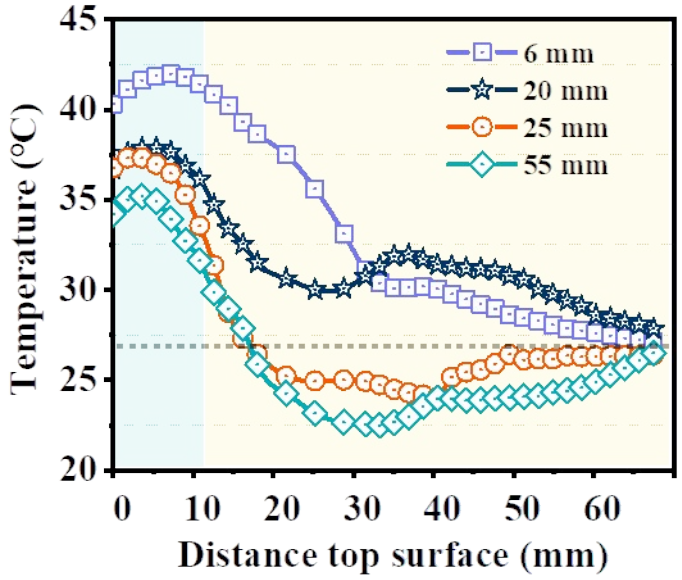

Figure S11. Temperature distribution on the side of the aerogel

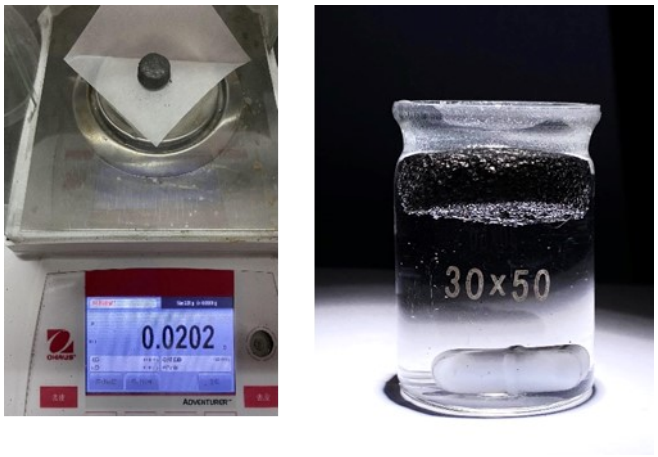

Figure S12. Photograph of weighing 20mg of aerogel and Sterilization process (20 mg of MFeG aerogel was floated in 20 mL of E. coli solution and placed on a magnetic stirrer)

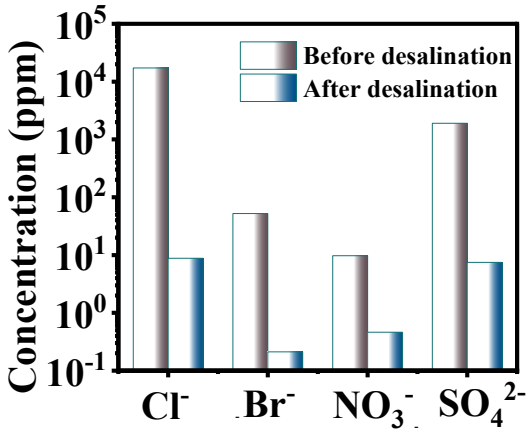

Figure S13. Concentrations of major ions in the seawater before and after desalination

Figure S14. Microscope images of emulsified oil before and after evaporation

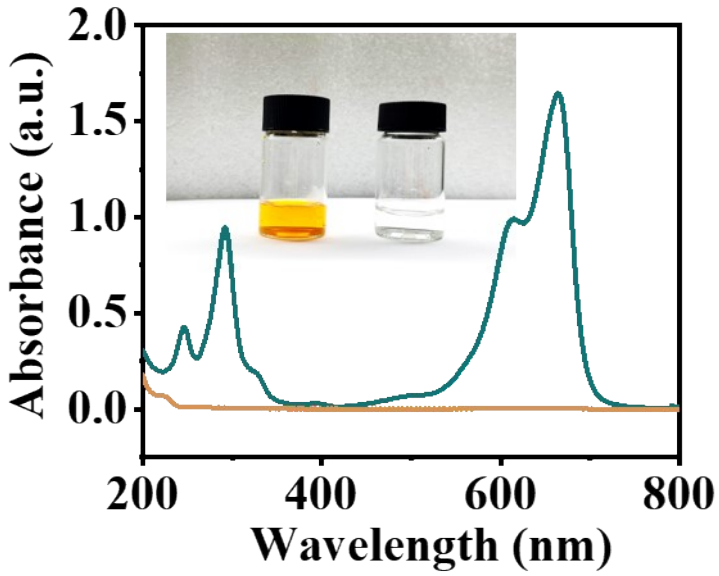

Figure S15. UV-Vis spectra of methyl orange before and after evaporation

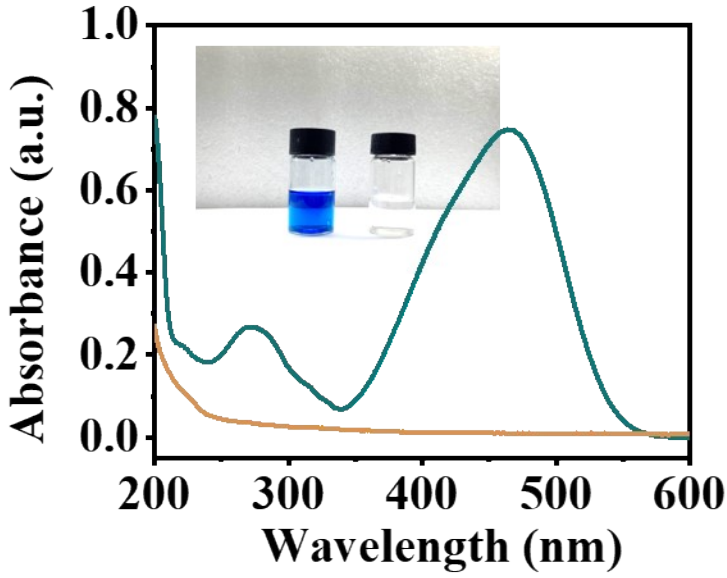

Figure S16. UV-Vis spectra of methylene blue before and after evaporation

Table S4. Comparison of 3D materials for water evaporation

3D Materials	Evaporation rate under 1 sun (kg/m^2 h)	Solar absorbance	Mechanism for highly-effective solar water evaporation	Ref.
3D GO/Mxene	1.27	-	excellent photothermal conversion, hierarchical water/vapor channels and efficient local energy management strategy	1
3D porous structure (rGO, CuS, CuO, PDA)	1.69	>95%	the side surfaces also contributed to the overall water evaporation	2
phthalocyanine derivative- PU foam	1.26	-	efficient sunlight absorption capacity, high photothermal conversion efficiency, good water transportation and thermal/photo-stability property	3
polydopamine-filled cellulose aerogel	1.36	~90%	unique porous structure, broad sun light absorption spectrum, and excellent photothermal conventional effect	4
3D bayberry tannin assembly of a graphene aerogel （BGA）	1.80	93.5%	BGA provides a larger area for water evaporation and a higher water transport rate	5
PAN/CNTs nanofiber based aerogels	2.13	94.8%	excellent light absorption, porous structure decreased water vaporization enthalpy	6
rGO /Ti_3C_2Tx MXene hydrogel	2.09	93.5%	A-RGO/MX hydrogel s anisotropic network enhances the multiple light absorption, decreasing the water vaporization enthalpy	7
N-doped reduced graphene oxide 3D aerogels	2.53	74.8%	interfacial evaporation, pyridinic and graphitic N-dopants greatly enhances the water transport and evaporation	8
3D rGO-cotton	2.95	97%	Cold evaporation surface between the solar evaporation surface and bulk water can extract energy from both sides	9
3D Patchy-surface hydrogel	4.0	93%	The increased thickness of the water layer in the hydrophilic region leads to the rapid escape of water molecule	10
polyimide/MXene aerogel	2.17	91.3%	array structure functions as effective thermal confinement, multi-directional mass transfer channels for fast water transport	11
$Ni1Co_3$@PDA-based sponges	2.42	>97.6%	The eliminated heat conduction loss, reduced radiation and convection loss, as well as net energy gain from the environment	12

Graphene and rice-straw-fiber-based aerogels	2.25	96–97%	3D photothermal aerogel effectively decreases the radiation and convection energy loss while enhancing energy harvesting from the environment	[13]
Au/N-doped rGO aerogel	2.72	99.7%	vertically aligned Au/graphene meshes with confined heat at micro and nanoscale levels	[14]
CNTs/BC/GBs/wood	2.9	>95%	the high light absorbance, effective thermal management, fast water transportation, and reduced vaporization enthalpy.	[15]
3D cup-shaped photothermal structure	2.6	∽91%	the inner wall gains energy by recovering the diffuse reflected light and thermal radiation from the bottom part, additional heat was gained from the ambient air when the 3D structure	[16]
Carbon-coated paper on polystyrene foam	2.20	-	extra energy taken from the warmer environment	[17]
Fe@Enteromorpha/graphene aerogel	3.85	∽95%	aerogel has good water transport capacity and local thermal localization, aerogel surface has an obvious cold evaporation effect	In this work

References

1 X. Ming, A. Guo, Q. Zhang, Z. Guo, F. Yu, B. Hou, Y. Wang, K. P. Homewood and X. Wang, *Carbon N. Y.*, 2020, **167**, 285–295.

2 B. Shao, X. Wu, Y. Wang, T. Gao, Z.-Q. Liu, G. Owens and H. Xu, *J. Mater. Chem. A*, 2020, **8**, 24703–24709.

3 X. Han, Z. Wang, M. Shen, J. Liu, Y. Lei, Z. Li, T. Jia and Y. Wang, *J. Mater. Chem. A*, 2021, **9**, 24452–24459.

4 Y. Zou, J. Zhao, J. Zhu, X. Guo, P. Chen, G. Duan, X. Liu and Y. Li, *ACS Appl. Mater. Interfaces*, 2021, **13**, 7617–7624.

5 F. Wu, D. Liu, G. Li, L. Li, L. Yan, G. Hong and X. Zhang, *Nanoscale*, 2021, **13**, 5419–5428.

6 Y. Liu, H. Liu, J. Xiong, A. Li, R. Wang, L. Wang, X. Qin and J. Yu, *Chem. Eng. J.*, 2022, **427**, 131539.

7 W. Li, X. Li, W. Chang, J. Wu, P. Liu, J. Wang, X. Yao and Z.-Z. Yu, *Nano Res.*, 2020, **13**, 3048–3056.

8 X. Meng, J. Yang, S. Ramakrishna, Y. Sun and Y. Dai, *ACS Sustain. Chem. Eng.*, 2020, **8**, 4955–4965.

9 Y. Wang, X. Wu, X. Yang, G. Owens and H. Xu, *Nano Energy*, 2020, **78**, 105269.

10 Y. Guo, X. Zhao, F. Zhao, Z. Jiao, X. Zhou and G. Yu, *Energy Environ. Sci.*, 2020, **13**, 2087–2095.

11 Y. Yang, W. Fan, S. Yuan, J. Tian, G. Chao and T. Liu, *J. Mater. Chem. A*, 2021, **9**, 23968–23976.

12 B. Shao, Y. Wang, X. Wu, Y. Lu, X. Yang, G. Y. Chen, G. Owens and H. Xu, *J. Mater. Chem. A*, 2020, **8**, 11665–11673.

13 D. P. Storer, J. L. Phelps, X. Wu, G. Owens, N. I. Khan and H. Xu, *ACS Appl. Mater. Interfaces*, 2020, **12**, 15279–15287.
14 X. Meng, J. Yang, S. Ramakrishna, Y. Sun and Y. Dai, *J. Mater. Chem. A*, 2020, **8**, 16570–16581.
15 Q.-F. Guan, Z.-M. Han, Z.-C. Ling, H.-B. Yang and S.-H. Yu, *Nano Lett.*, 2020, **20**, 5699–5704.
16 Y. Shi, R. Li, Y. Jin, S. Zhuo, L. Shi, J. Chang, S. Hong, K.-C. Ng and P. Wang, *Joule*, 2018, **2**, 1171–1186.
17 H. Song, Y. Liu, Z. Liu, M. H. Singer, C. Li, A. R. Cheney, D. Ji, L. Zhou, N. Zhang, X. Zeng, Z. Bei, Z. Yu, S. Jiang and Q. Gan, *Adv. Sci.*, 2018, **5**, 1800222.